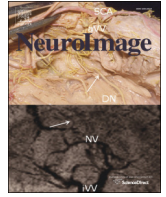




Contents lists available at SciVerse ScienceDirect

NeuroImage

journal homepage: www.elsevier.com/locate/ynimg

Review

Localizing the human primary auditory cortex in vivo using structural MRI

Christian Wasserthal^a, André Brechmann^{a,*}, Jörg Stadler^a, Bruce Fischl^{b,c}, Karin Engel^a

^a Special-Lab Non-Invasive Brain Imaging, Leibniz-Institute for Neurobiology Magdeburg, Germany

^b Athinoula A Martinos Center, Dept. of Radiology, MGH, Harvard Medical School, MA, USA

^c MIT HST/Computer Science and AI Lab, MA, USA

ARTICLE INFO

Article history:
Accepted 16 July 2013
Available online xxxx

Keywords:
Human primary auditory cortex
Localization
In vivo
MRI

ABSTRACT

Currently there are no routine methods to delineate the primary auditory cortex (PAC) of humans in vivo. Due to the large differences in the location of the PAC between subjects, labels derived from post-mortem brains may be inaccurate when applied to different samples of in vivo brains. Recent magnetic resonance (MR) imaging studies suggested that MR-tissue properties can be used to define the location of the PAC region in vivo. The basis for such an approach is that the PAC region is more strongly myelinated than the secondary areas. We developed a fully automatic method to identify the PAC in conventional anatomical data using a combination of two complementary MR contrasts, i.e., T1 and T2, at 3 T with 0.7 mm isotropic resolution. Our algorithm maps the anatomical MR data to reconstructed cortical surfaces and uses a classification approach to create an artificial contrast that is highly sensitive to the effects of an increased myelination of the cortex. Consistent with the location of the PAC defined in post-mortem brains, we found a compact region on the medial two thirds of Heschl's gyrus in both hemispheres of all 39 subjects. With further improvements in signal-to-noise ratio of the anatomical data and manual correction of segmentation errors, the results suggest that the primary auditory cortex can be defined in the living brain of single subjects.

© 2013 Published by Elsevier Inc.

Contents

| | |
|---|---|
| Introduction | 0 |
| Material and methods | 0 |
| Concept of mapping | 0 |
| Image acquisition | 0 |
| Segmentation and surface reconstruction | 0 |
| Volume-to-surface mapping | 0 |
| Properties of the feature space | 0 |
| Mapping the differences in the likelihood of increased myelin content | 0 |
| Optimization | 0 |
| Analysis of the mapping results | 0 |
| Evaluation of the PAC estimate | 0 |
| Results | 0 |
| Robustness of the classification algorithm | 0 |
| Shape, anatomical location and spatial extent of the PAC estimate | 0 |
| Discussion | 0 |
| Conclusion | 0 |
| Acknowledgment | 0 |
| References | 0 |

* Corresponding author at: Leibniz Institute for Neurobiology, Special-Lab Non-Invasive Brain Imaging, Brenneckestr. 6, 39118 Magdeburg, Germany. Fax: +49 391 626392589.
E-mail address: brechmann@lin-magdeburg.de (A. Brechmann).

Introduction

The knowledge of the exact location and delineation of cortical areas in the living human brain would benefit the interpretation of activation obtained using functional imaging methods such as functional magnetic resonance imaging (fMRI) and positron emission tomography (PET). Currently functional imaging studies mostly rely on parcellation schemes that have been obtained from post-mortem brains using architectonic methods (e.g., Brodmann, 1909; von Economo and Koskinas, 1925). The scheme of Brodmann (1909) has been implemented into standard brain templates such as the Talairach atlas which is based on one brain or the Montreal Neurological Institute (MNI) which is based on an average of more than 100 brains. However, the precision of the location of cortical brain areas, which have been defined in only a few brains, is limited because of the large anatomical differences between subjects. A current approach to overcome this problem is to use surface-based alignment of the cortical folding patterns (Fischl et al., 2008) or template-free registration (Tahmasebi et al., 2009) in conjunction with probability maps that are based on newly defined architectonic properties of cortical areas in ten different brains (Mazziotta et al., 2001; Zilles et al., 2002). The results suggest that cortical folds are much better predictors of the cytoarchitecturally defined regions than had been previously thought. Therefore this approach is extremely valuable for group analyses of brain imaging studies. However, it may still fail when applied to brain activity of individual subjects and even groups of subjects if the cortical area of interest is small, and it seems useful to acquire additional information to robustly localize specific brain regions in individual brains. In the visual system, such additional information has been obtained from retinotopic mapping experiments (e.g., Sereno et al., 1995). In addition, anatomical information from individual subjects can be used to estimate the shape of primary visual cortex as recently suggested by Hinds et al. (2008). In the auditory modality, however, comparable routine methods are not available, and recent attempts to prove the mirror-symmetric tonotopic organization of the primary auditory cortex (PAC) areas using high resolution fMRI showed contradictory results (Da Costa et al., 2011; Dick et al., 2012; Formisano et al., 2003; Humphries et al., 2010; Langers et al., 2007; Moerel et al., 2012; Schonwiesner et al., 2002; Striemi-Amit et al., 2011; Talavage et al., 2004; Woods et al., 2009). Thus, even the localization of the primary auditory cortex areas of humans and even more so its delineation from the neighboring areas is still an unsolved issue. The consequence is that activation observed on or near Heschl's gyrus (HG) in functional imaging studies is often attributed to primary auditory cortex irrespective of its exact location. This is misleading even more so when coordinates of the primary auditory cortex (Brodmann area 41) in Talairach or MNI brain templates are used. From a number of architectural parcellation schemes (Beck, 1930; Clarke and Rivier, 1998; Flechsig, 1908; Galaburda and Sanides, 1980; Hopf, 1954a,b; Morosan et al., 2001; von Economo and Horn, 1930), it is evident that a large number of functionally separate fields occupy Heschl's gyrus and its immediate vicinity. If the functional parcellation scheme of the core and medial and lateral belt areas that are known from the monkey (see Hackett et al., 2001; Kaas and Hackett, 1998) also applies to the human auditory cortex, about ten of such fields are to be expected (i.e., the primary areas A1, R and RT, the medial belt areas CM, RM, RTM, and the lateral belt areas CL, ML, AL, RTL). To better understand the processing in these primary and secondary areas, routine methods are needed to delineate these areas in humans in vivo.

In recent years anatomical MR imaging has been used to determine fine grain differences in tissue properties in post-mortem material (e.g., Fischl et al., 2008). First attempts have also been made in vivo mainly to delineate the primary visual cortex (Bridge et al., 2005; Duyn et al., 2007; Eickhoff et al., 2005). An anatomical imaging approach has been suggested by Sigalovsky et al. (2006) by mapping an intrinsic MR property, i.e. the longitudinal relaxation rate (R1), of gray matter in auditory cortex. The basis for such a

definition is that the gray matter of primary areas is more strongly myelinated than that of secondary areas. In high resolution MR images of post-mortem tissue such differences can be observed (Fig. 1A), but in vivo images of humans must be acquired at a much lower resolution such that the fine grain details of tissue MR contrast are much less evident (Figs. 1B,C).

Sigalovsky et al. (2006) showed the distribution of R1 values within the auditory cortex of a limited number of five subjects scanned at 1.5 T at $1.3 \times 1.0 \times 1.3 \text{ mm}^3$ resolution. In most of the hemispheres they found the highest R1 values in posteromedial Heschl's gyrus, which is consistent with the location of PAC in architectural studies. However, in four out of five subjects they obtained large areas with similar relaxation rates on the planum temporale, which have not been described in any of the histological studies and are thus a matter of debate.

The aim of the current study was to identify the human primary auditory cortex (PAC) area as defined in human architectonic studies, e.g., Brodmann area 41 (Brodmann, 1909), area TC (von Economo and Horn, 1930) or area Te1 (Morosan et al., 2001). We follow a fully automatic approach of combining two different, complementary MR contrasts, i.e., T1 and T2 weighted anatomical imaging, of 39 brains at 3 T with 0.7 mm isotropic resolution. These reflect both longitudinal and transversal relaxation properties of brain tissue. Compared to using only one contrast, this combination will thus be more reliable for identifying the PAC in individual subjects and reduce the labeling of non-PAC areas, i.e., on planum temporale. This was also recently shown by Glasser and Van Essen (2011) using a global approach to combine T1 and T2 weighted MRI. Here, we propose a novel data-driven technique to map the differences in the likelihood of increased myelin content in the primary auditory cortex and adjacent higher-order regions.

In contrast to previous work, our mapping approach is based on a local, unsupervised classification technique. It takes into account the limitations of MR imaging as well as the variability of the auditory cortex anatomy without having to resort to model-based or interactive outlier removal, non-linear transformations and extensive low pass filtering of the data. This ensures the reliability and reproducibility of the mapping results. Another important advantage is that our method can be easily extended to compare the feature distributions of further regions as well as to combine information from any number of different measurements. For example, the method may in the future be adapted to delineate functional areas within and outside the PAC by considering additional, complementary MR scans as input, such as susceptibility weighted imaging and angiography data or functional activation maps.

We carefully analyze the reliability of the estimated PAC regions in the individual brains based on anatomic definitions of the human auditory cortex (Brodmann, 1909; Morosan et al., 2001; von Economo and Horn, 1930) and investigate the robustness of our approach.

A true validation of the individual localization results would require additional information, in particular functional measurements that reveal stable, comparable patterns of the functionally separate fields, such as tonotopy. Unfortunately, irrespective of the ongoing attempts at parcellating the auditory cortex based on topographic maps (e.g., Da Costa et al., 2011; Dick et al., 2012), the robust localization and precise delineation of the human PAC areas in vivo remain elusive, as recently summarized by Moerel et al. (2012): "To date, it remains unclear how the location and orientation of the auditory core relates to these tonotopic gradients. Several imaging studies suggested that the primary tonotopic gradient is oriented in posteromedial to anterolateral direction along HG (Formisano et al., 2003; Riecke et al., 2007; Seifritz et al., 2006). Conversely, recent studies argued that the main gradient runs in anterior–posterior direction (Da Costa et al., 2011; Humphries et al., 2010; Striemi-Amit et al., 2011)". Unfortunately, no tonotopic results are available that describe individual or group maps in standard space. These limitations complicate the interpretation and empirical evaluation of functionally separate fields by a comparison with different in-vivo topographic maps. Hence, despite their inherently limited use for a precise localization of the human PAC areas, 190

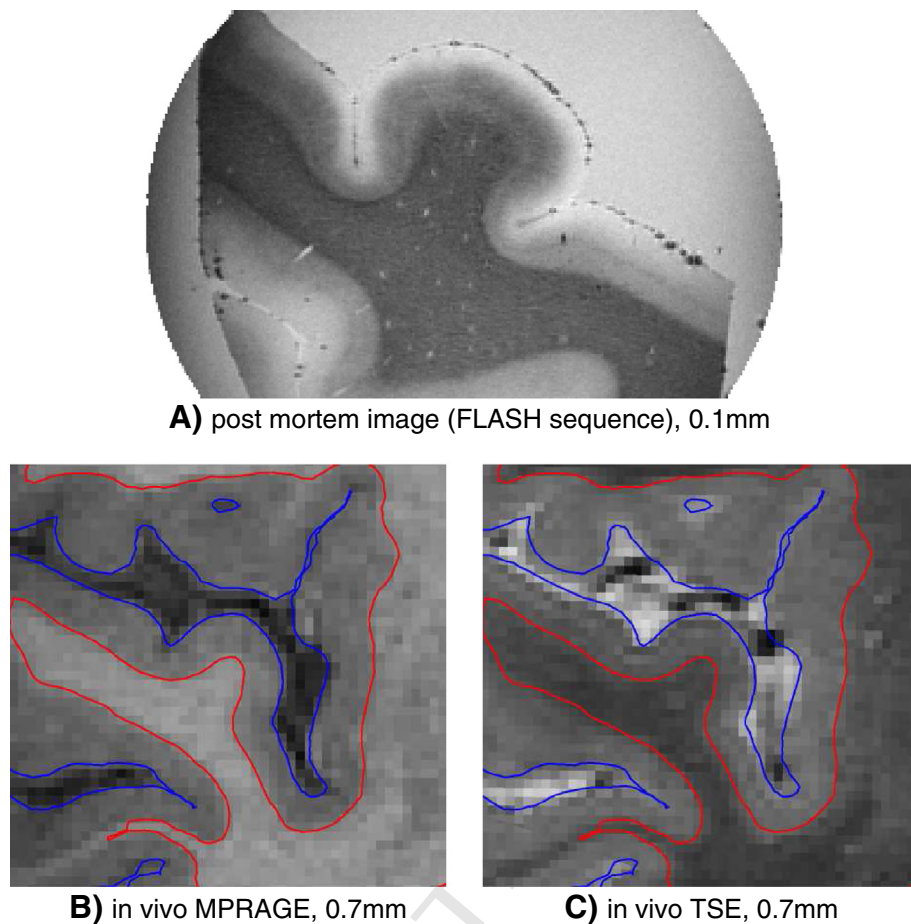


Fig. 1. Post mortem tissue scanned at 0.1 mm with a FLASH sequence (A) and the two contrasts we acquired for our study (B–C). Each image is in coronal orientation and centered to Heschl's gyrus. In (A) the lower two thirds of the gray matter in this region clearly show a shift in intensity similar to the white matter. This, however, is not apparent in the in vivo images. Also note that the lower layers seem to be compressed within deep sulci left and right of Heschl's gyrus in panel (A).

191 architectonic probability maps must currently be considered as state of
 192 the art, with which we compare our in vivo group maps, i.e., to the prob-
 193 ability maps of the PAC region from the ex vivo studies by Morosan et al.
 194 (2001).

195 Material and methods

196 Concept of mapping

197 The presented algorithm generates from $d \geq 1$ MR measurements
 198 per subject a cortical surface overlay that reveals individual differences
 199 in the local cortical myelination. Highlighted regions in the in vivo maps
 200 can be understood as brain regions with a high likelihood of increased
 201 myelin content similar to that of the primary cortex region of interest.

202 For the purpose of localizing the PAC in the in vivo maps, we acquired
 203 anatomical MR images with two different contrasts ($d = 2$). For each
 204 subject and hemisphere we generated a reconstruction of the inner
 205 (i.e., gray–white matter) and outer (i.e., gray matter–CSF) cortical bound-
 206 ary in the form of triangle meshes. The MR intensities perpendicular to
 207 the inner cortical boundary were then mapped to these surfaces. The
 208 MR contrasts (T1 and T2) provide partial, indirect and complementary in-
 209 formation about average myelin density. By combined analysis of the MR
 210 feature distribution the differences in tissue properties between Heschl's
 211 gyrus and adjacent areas are boosted by using a statistical classifier.

212 Unlike with previous work, we propose an unsupervised, local ap-
 213 proach that provides a robust, reproducible, data-driven classification of
 214 the MR intensities, and implies a reliable estimate of the individual loca-
 215 tion and shape of the PAC region. Each individual PAC area can be defined

by analyzing in the resulting surface overlays the spatial layout of
 highlighted patches in the temporal lobes of each of the cortical hemi-
 spheres under study. In each case, the final classification result is obtained
 by iteratively optimizing the separability of the two different MR feature
 distributions that are estimated based on the local feature samples from a
 compact, ellipsoid sampling region over the subject's Heschl's gyrus and
 an adjacent sampling region that more likely covers other cortex areas
 within the subject's temporal lobe. The ellipsoid embeddings of the sam-
 pling regions are initialized by mapping the Heschl's gyrus label from a
 standard atlas to the single cortical surfaces, and labeling the surrounding
 surface region, respectively. These sampling regions are then iteratively
 deformed until the overlap of the two local distributional estimates in
 the feature space is minimized. Finally, the optimal decision boundary
 is used to compute the cortical surface overlays, and highlighted, hyper-
 intense surface regions overlapping the deformed ellipsoids are consid-
 ered as the most likely in vivo estimates of the human PAC area.

Our algorithm avoids extensive, model-based improvements of the
 raw data. That is, possible artifacts due to imaging limitations and
 (pre-) processing error are taken into account, but outliers are currently
 neither explicitly modeled nor removed. The chosen regularization con-
 straints follow basic anatomical knowledge about myelin distribution,
 cortex anatomy and structure–function relationships that do not intro-
 duce a strong bias.

Image acquisition

In this study, we used two specific MR contrasts, namely T1 weighted
 MPRAGE (Magnetization-Prepared Rapid Acquisition Gradient Echo)

and T2 weighted TSE (Turbo Spin-Echo). These two protocols have been chosen because of their myelin sensitivity, and give a good gray/white matter contrast.

We acquired data of 39 subjects in a 3 T scanner (Siemens Trio) using an 8-channel head coil for RX and a body coil for TX. While the typical resolution for structural MRI is 1 mm, we decided to scan at a higher resolution in order to reduce partial volume effects. More specifically, the MPRAGE images were acquired with an isotropic spatial resolution of 0.7 mm ($TR = 2500$ ms, $TE = 4.94$ ms, $TI = 1100$ ms, 7° flip angle, matrix size $320 \times 320 \times 256$, bandwidth = $140 \frac{\text{Hz}}{\text{px}}$, 1 average), and the TSE images were scanned with 0.7 mm isotropic resolution ($TR = 3000$ ms, $TE_{\text{eff}} = 355$ ms, matrix size $320 \times 320 \times 256$, bandwidth = $520 \frac{\text{Hz}}{\text{px}}$, ETL = 161, 1 average). Both scans were acquired for each subject in one session in about 14 and 18 min respectively.

Field maps have not been acquired. The product sequences were changed in matrix size and FOV (given by matrix size and pixel resolution), without applying pre-scan normalization.

Segmentation and surface reconstruction

Segmentations and cortical surface reconstructions were obtained from the MPRAGE images using the FreeSurfer toolkit (FST). This included by default the re-sampling of the data to 1 mm isotropic resolution, brain extraction, intensity normalization and surface topology correction (for an overview of the underlying algorithms and procedures see Dale et al., 1999; Fischl et al., 1999a, 2001; Ségonne et al., 2004).

The surfaces generated by FreeSurfer share the same topology and differ only in their spatial embedding. That is, each mesh vertex is identified via a unique label, and is defined at different coordinates, e.g., on the white/gray matter boundary, the gray matter–CSF boundary and on the inflated mesh.

One important aspect of FreeSurfer's MGZ file format is that the available metadata supports the transformation of each individual brain into a normalized space without modifying the underlying data. For example, the spherical registration w.r.t. the anatomical information present in the "fsaverage" surface modifies the spatial embedding of the surface meshes only. Moreover, it allows registering the MPRAGE image with the TSE image of each subject without re-sampling (i.e., by running `spmregister` and `mri vol2vol` with the attribute `no-resample`). From our experience, an affine transformation of the different brain scans provides sufficient accuracy of the co-registration. Severe differences were not identified by manual inspection using the surface overlays. If the image distortion is low (or similar for both contrasts), the cortical surfaces generated by FreeSurfer will then fit both data sets (see Figs. 1B and C). Other cases should be excluded, or the distortions should be corrected, which was not necessary in the present study.

Volume-to-surface mapping

Our method uses the cortical surfaces for two main reasons. First, the surfaces provide a compact representation and more reliable estimates for the spatial extent and relations of the identified brain regions on the folded cortex. For example, we will use the surfaces in their inflated configurations for visualization purposes. Compared with the original, anatomically correct surfaces, the inflated versions are less occlusive.

Second, it allows us to use the anatomical knowledge that the cortex is a highly folded sheet of gray matter with an average thickness of 2–4 mm and a spatially variant columnar and laminar organization to reduce the complexity of the input data prior to analysis (Fischl and Dale, 2000).

In the cortex-based representation of the MR intensities one value per MR contrast is assigned to each surface vertex. In order to obtain an accurate representation, our mapping approach samples the MR volumes in surface normal direction. It uses orthogonal profile lines from the vertices of the inner cortical surface (see Fig. 2A), and samples the MR intensities along these profile lines at 20 equidistant points. These samples are then averaged in order to generate a value that is representative for the MR intensity of the gray matter over this vertex. The length of each of these profiles is chosen in accordance with the local cortical thickness estimated by FreeSurfer (Fischl and Dale, 2000) and determines the local scale of the weighting function.

In order to emphasize intensities of the inner two thirds of the gray matter and minimize partial volume effects at the border of the gray matter, these values are combined using a Gaussian weighting function centered on the sixth sample point, see Fig. 2B. Taking samples at 20 equidistant points gives a good trade-off between the numerically optimal approximation of a Gaussian kernel and computational efficiency.

The resulting mapping of the two MR volumes (MPRAGE and TSE) to the cortical surfaces is exemplarily shown for one subject in Figs. 3A and C.

Properties of the feature space

After the MR values were mapped to the surface vertices, each vertex provides a sample \vec{x} in a d -dimensional feature space. Here, $d = 2$, i.e., this space is spanned by the intensities of the two MR contrasts we acquired.

The resulting feature space cannot be readily analyzed by using a global, unsupervised approach, because intensity variations within the gray matter due to different contribution of the receiver coils and magnetic field inhomogeneities may outweigh the intensity variations caused by the regionally varying cortical myelination. The standard

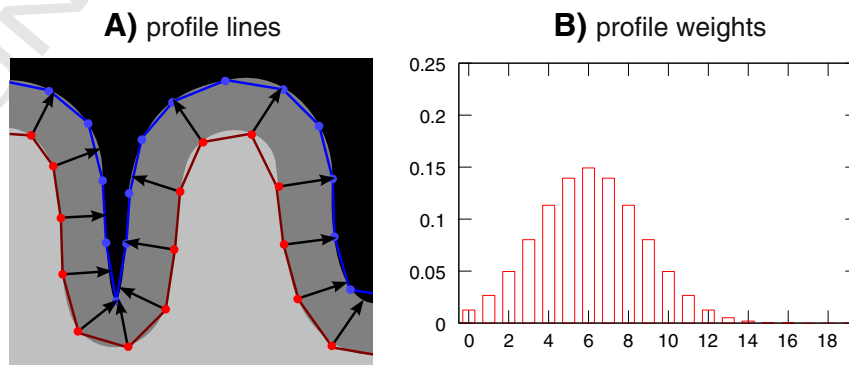


Fig. 2. This figure illustrates the surface mapping by stochastic sampling of the MR volumes. Panel (A) shows how transcortical profiles lines were defined, and panel (B) shows how the values sampled along these profile lines were weighted (B). The x-axis in (B) indicates the relative position of the sample, zero denoting the start point on the gray–white matter interface and 19 the last point on the pia mater. The kernel weights are given at the y-axis.

330 practice of correcting shading artifacts by employing a model of intensity
 331 variations within the different tissue types and experimental estimates
 332 of the transmit and receive field inhomogeneities may, however, intro-
 333 duce its own bias. To address this problem, rather than modifying the
 334 raw data, we take advantage of one important property of these inhomog-
 335 eneities, namely their low spatial frequency. As indicated by our results,
 336 the sensitivity to uncertainty in the intensity variations can be effectively
 337 reduced by restricting the feature space analysis to spatially compact
 338 regions.

339 We therefore define two sampling regions on the surfaces, R_{in} and
 340 R_{out} . As exemplarily shown in Fig. 3, these regions are compact and of
 341 sufficiently small size regarding the cortex region of interest. Intensity
 342 variations caused by magnetic field inhomogeneities within and be-
 343 tween these two regions are negligible compared with the global varia-
 344 tions, and should not have a significant effect on the performance of the
 345 statistical classifier. The inner region R_{in} is based on the anatomical label
 346 “transversetemporal” generated by FreeSurfer (Desikan et al., 2006;
 347 Fischl et al., 2004). It represents Heschl’s gyrus, whereas the surround-
 348 ing sampling region R_{out} is defined as a dilated version of the former.

349 These regions do not primarily define the anatomical search space,
 350 but imply an initial classification of the samples that is sufficiently ro-
 351 bust to regionally varying cortical myelination due to shading. More-
 352 over, if Heschl’s gyrus has been properly labeled in the individual
 353 cortical surfaces, the induced classifier allows the distinguishing of sam-
 354 ples taken from the two differently myelinated tissue classes within the
 355 PAC and adjacent non-PAC areas.

356 Fig. 5 shows a plot of the distribution of feature vectors from both
 357 initial regions. Evidently, the samples taken from the inner region (col-
 358 ored in green) are shifted towards increased MPRAGE and decreased
 359 TSE intensities compared to the samples taken from R_{out} . As the inner
 360 region is initialized using the “transversetemporal” gyrus label, this ob-
 361 servation is in accordance with our presumption of an increased myelination of the PAC, which is related to this gyrus.

363 Our results indicate that the automatic, atlas-based approach pro-
 364 duces sufficiently accurate and robust initializations for the unsupervised
 365 tissue classification.

366 The two MR contrasts only provide partial, indirect information
 367 about the myelin content, which can be used to delineate the core
 368 areas of the auditory cortex. These presumably comprise three fields
 369 according to the myeloarchitectonic literature (e.g., Beck, 1930;
 370 Hackett et al., 2001; Kaas and Hackett, 1998; Morosan et al., 2001;
 371 Wallace et al., 2002), which show only subtle differences in myelin con-
 372 tent. As indicated by the dashed isolines in Fig. 5, the MR contrasts re-
 373 veal clear differences in myelin content between the highly
 374 myelinated primary auditory cortex and the less densely myelinated
 375 higher order areas adjacent to the PAC. Thus, rather than implying a
 376 parcellation into the multiple functionally different auditory cortex
 377 fields, the desired classifier will optimally separate the two clusters
 378 ($k = \{in, out\}$) in the feature space that correspond to the highly mye-
 379 linated PAC and the less densely myelinated non-PAC areas.

380 Mapping the differences in the likelihood of increased myelin content 380

381 Using the feature space that is defined by the projected MR intensi-
 382 ties and the two predefined surface regions, the parameters of a multi-
 383 variate normal distribution $N_k(\mu_k, \Sigma_k)$ can be estimated for each of the
 384 classes $k = \{in, out\}$. With these distributions it is possible to assign to
 385 each surface vertex a likelihood for following the distribution L_{in} of fea-
 386 tures from the inside class (i.e., showing MR intensities similar to those
 387 within the highly myelinated PAC region), or the outside distribution
 388 L_{out} (i.e., representing dissimilar MR intensities). Therefore, we evaluate
 389 the probability density function,

$$L_k(\vec{x}) = \frac{1}{\sqrt{(2\pi)^d |\Sigma_k|}} \exp\left(-\frac{1}{2}(\vec{x} - \vec{\mu}_k)^\top \Sigma_k^{-1} (\vec{x} - \vec{\mu}_k)\right), \quad (1)$$

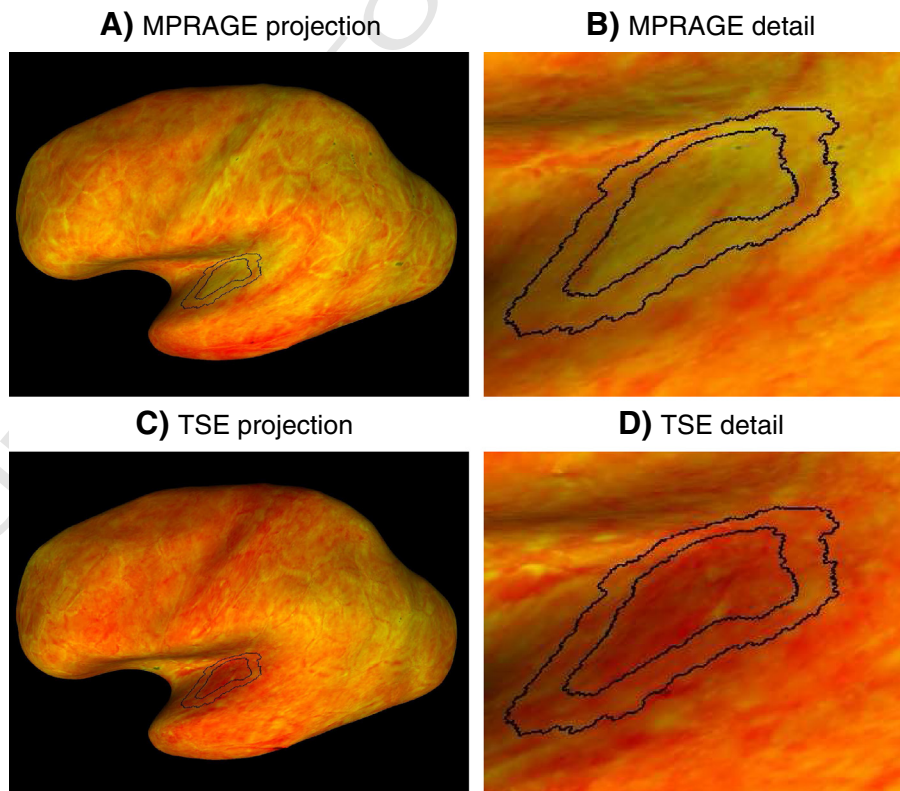


Fig. 3. This figure shows the values of MPRAGE (A) and TSE (C) computed for the left hemisphere of one representative subject, and projected onto the inflated inner cortical surface. Panels (B,D) show a portion of the maps centered at the estimated location of the transverse temporal gyrus in detail. The heat scale used for the MPRAGE and TSE values uses red for low and yellow for high intensities. The black lines indicate the boundaries of the initial regions R_{in} and R_{out} (cf. Properties of the feature space section).

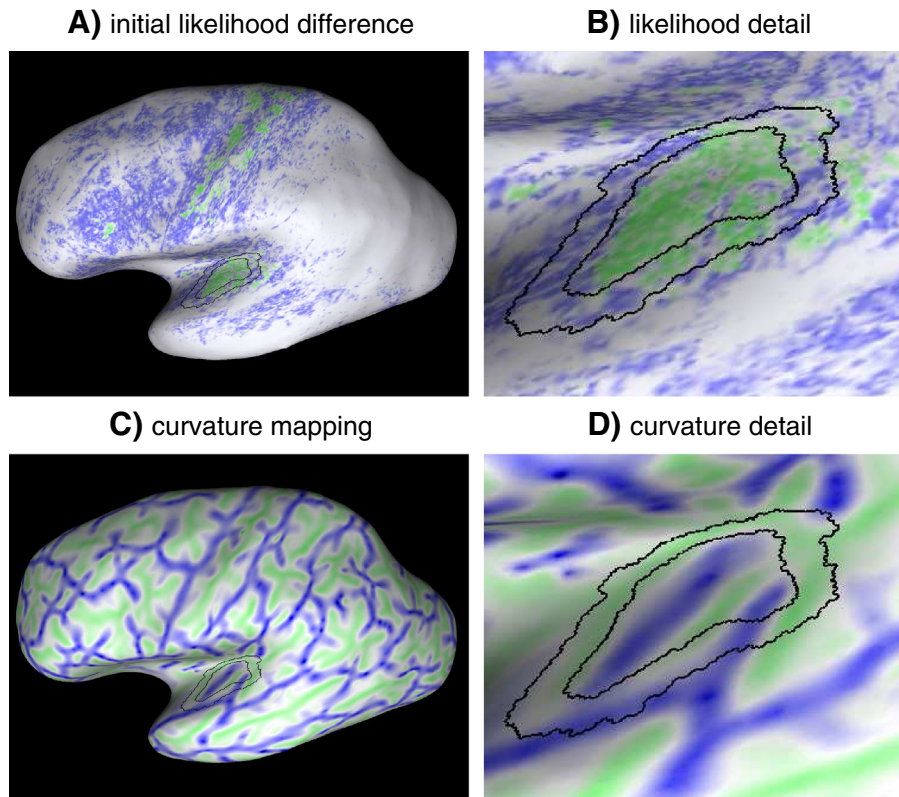


Fig. 4. This figure shows the initial likelihood difference map (A) and the curvature map due to the embedding of the cortical sheet in 3D (C) for the left hemisphere shown in Fig. 3. Panels (B,D) show a portion of the maps centered at the transverse temporal gyrus. The color scale in the likelihood-difference map uses blue for negative, white for values near zero and green for positive values. In panels (C-D) green color indicates positive curvature values (i.e., gyri) and blue color indicates negative curvature (i.e., sulci). The black contours represent the boundaries of the sampling regions.

where d is the number of dimensions of the feature space (in our case $d = 2$).

The values $L_{in} - L_{out}$ allow a visual representation of the properties of the initial feature space in a convenient manner. For example, Figs. 4A and b provide a visual display of the map resulting from the classification in terms of a surface overlay, which is referred to as likelihood-difference map. The likelihood-difference will be positive (colored in green) if a feature vector is better represented by the inside distribution L_{in} , negative (i.e., blue) if it is better represented by the outside distribution L_{out} , or close to zero (i.e., white) if both distributions fit equally well.

In order to avoid numerical problems, we use the difference in the values L_{in} and L_{out} instead of log-likelihood or likelihood ratios for computing the classification (inside, outside and neither).

As a consequence of our local analysis it will be highly probable that likelihood-difference values close to zero represent features fitting neither of the distributions. If the feature values are – due to global inhomogeneities – not comparable to the locally estimated gray value distributions, both likelihoods (L_{in} and L_{out}) will be close to zero for many vertices on the surface. Thus, taking the likelihood-difference does not allow for the global analysis of the myelin distribution, but greatly reduces the risk of false positive tissue classifications at the local basis. That is, the likelihood-difference may or may not allow a complete and detailed parcellation of the cortex, but will significantly differ locally between the estimated PAC and non-PAC areas.

Optimization

Our algorithm compares the two distributions drawn from the regions R_{in} and R_{out} . A classifier amplifies the regions' complementary properties being represented by MR intensities, which are sensitive to myelination. It is therefore critical that the regions are initialized in a way that the inside region will overlap the PAC to a higher degree than the outside region, i.e., contains more samples from the higher myelinated cortical region. This condition is easily fulfilled by the gyrus label “transversetemporal” provided by FreeSurfer. The PAC is known to mainly reside on the first transverse temporal gyrus, called Heschl's gyrus (HG) and the location of HG can therefore be used as an anatomical landmark for setting up the initial sampling region R_{in} in each of the cortical hemispheres under study. The exact shape and extent of the PAC in relation to this simple estimate of a compact and the higher myelinated area along HG are, however, not known in individual subjects. Moreover, the initial estimate may be very weak because the quality of

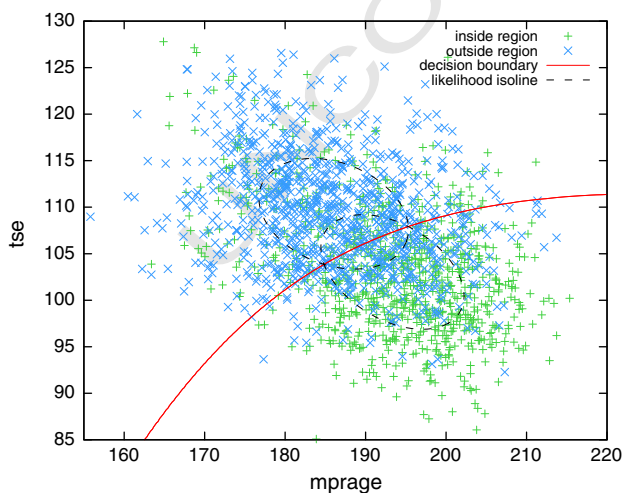


Fig. 5. Initial feature space due to the atlas labeling of the “transversetemporal” gyrus (matching Figs. 3, 4). The shapes of the estimated feature distributions within the inner and outer sampling regions are indicated by dashed isolines. The decision boundary that is imposed by the initial distributional estimates is indicated by the red contour.

431 the anatomical labeling highly depends on the anatomical information
 432 in the FreeSurfer atlas, which may not be representative for every sub-
 433 ject. That is why the individual PAC estimate is refined in a data-
 434 driven optimization.

435 We use an iterative process for simultaneously optimizing the place-
 436 ment of the regions (R_{in} and R_{out}), the resulting likelihood estimates and
 437 induced classifier. The optimization is implemented as a gradient ascent
 438 in parameter space using the Jensen–Shannon divergence as a criterion.

439 More precisely, we evaluate the separability of the two probability
 440 density functions, which are estimated based on the classification indu-
 441 ced by the regions R_{in} and R_{out} . It is defined as the Jensen–Shannon di-
 442 vergence between two multivariate normal distributions (Bar-Hillel
 443 et al., 2006), which is given by

$$D_{JS} = \frac{1}{2} \left(\ln |\Sigma^*| - \frac{1}{2} \ln |\Sigma_{in}| - \frac{1}{2} \ln |\Sigma_{out}| \right), \text{ with}$$

$$\Sigma^* = \sum_{k \in \{in, out\}} \frac{1}{2} \left(\Sigma_k + (\bar{\mu}_k - \bar{\mu}^*)(\bar{\mu}_k - \bar{\mu}^*)^T \right) \text{ and} \quad (2)$$

$$\bar{\mu}^* = \sum_{k \in \{in, out\}} \frac{1}{2} \bar{\mu}_k.$$

444 The region R_{in} is represented as the intersection of an ellipsoid with
 445 the inflated surface. This ellipsoid w is defined by the parameter vector

$$w = (\bar{c}, \vec{v}_a, \vec{v}_b, \vec{v}_c, a, b, c),$$

449 where the center point (\bar{c}) is given by the coordinates of a vertex of
 450 the inflated surface; three orthogonal unit vectors define the main
 451 axes (\vec{v}_a, \vec{v}_b and \vec{v}_c) with lengths a, b and c . As R_{out} is a function of
 452 the inner region, it has no degrees of freedom (see below).

453 The parameter values at iteration $m \geq 0$ are denoted w_m . Initially
 454 ($m = 0$), we define the center vertex \bar{c} to be the surface point closest
 455 to the center of mass given by the coordinates of vertices assigned to
 456 the aparc label “transversetemporal”. To initialize the axes’ orientation
 457 and length, we use the eigenvectors $\{\vec{e}_i\}$ and eigenvalues $\{\lambda_i, i =$
 458 $1, 2, 3\}$, of the covariance matrix Σ of the coordinates of the labeled verti-
 459 ces. That is,

$$\vec{v}_a = \vec{e}_1, \vec{v}_b = \vec{e}_2, \vec{v}_c = \vec{e}_3,$$

$$a = 2\sqrt{\lambda_1}, b = 2\sqrt{\lambda_2}, c = 2\sqrt{\lambda_3}.$$

462 The separability criterion (2) is then iteratively maximized by find-
 464 ing in each step the value

$$w_{m+1} = \arg \max_{w' \in h(w_m)} D_{JS}(w'_m),$$

466 i.e., by applying perturbations h to the parameter values w_m of the ellip-
 468 soid embedding known from the previous iteration. The iterative pro-
 469 cess stops if no further improvement is being made (i.e., $w_{m+1} =$
 470 w_m). The function h for changing the center point coordinates, rotating
 471 and adjusting the lengths of the main axes of an ellipsoid with param-
 472 eters w_m is given by

$$h(w_m) = \left\{ w_m, (\vec{v}, \vec{v}_a, \vec{v}_b, \vec{v}_c, a, b, c), \right. \\ \left. (\bar{c}, \vec{v}_a \cdot R, \vec{v}_b \cdot R, \vec{v}_c \cdot R, a, b, c), \right. \\ \left. (\bar{c}, \vec{v}_a, \vec{v}_b, \vec{v}_c, da, b, c), \right. \\ \left. (\bar{c}, \vec{v}_a, \vec{v}_b, \vec{v}_c, a, db, c), \right. \\ \left. (\bar{c}, \vec{v}_a, \vec{v}_b, \vec{v}_c, a, b, dc) \right\}, \text{ with}$$

$$\vec{v} \in \{ \vec{v} : \vec{v} \text{ adjacent to } \bar{c} \},$$

$$R \in \{ R_x(\phi), R_y(\phi), R_z(\phi) \} \text{ and } \phi \in \{ 2^A, -2^A \},$$

$$d \in \{ 0.8, 1.2 \}.$$

476 In order to evaluate the divergence $D_{JS}(w'_m)$, the regions R_{in} and R_{out}
 477 have to be reconstructed in each iteration based on the estimates w_m .
 478 As before, the inner region R_{in} is generated by intersecting the
 479 reconstructed ellipsoid with the inflated surface. R_{out} is determined by
 480 expanding R_{in} using a vertex-based dilatation. If the resulting surface
 481 patch R_{out} has approximately twice the size of the inner region, R_{in} is re-
 482 moved from the outer region.

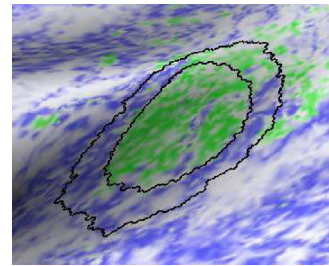
484 Analysis of the mapping results

485 The likelihood-difference maps can be directly used for the systemat-
 486 ic evaluation of the method as well as for the validation and compar-
 487 ison of the localization results with anatomic definitions of the PAC (see
 488 Figs. 7–10).

489 In the present study, we also investigated the robustness of the
 490 proposed classification approach to initialization and optimization
 491 (i.e., sampling and weighting) parameters. An extensive further evalua-
 492 tion of a possible bias due to imaging and model errors, e.g., in the pre-
 493 processing steps of the FreeSurfer pipeline, further improvements and
 494 fine-tuning of the mapping approach will be subject to future work.

495 A histogram analysis has been performed to assess the robustness of
 496 the optimization to the initial anatomical labeling of the gyrus-based
 497 (“transversetemporal”) region of interest (cf. Desikan et al., 2006). The

A) final likelihood difference



B) final feature space

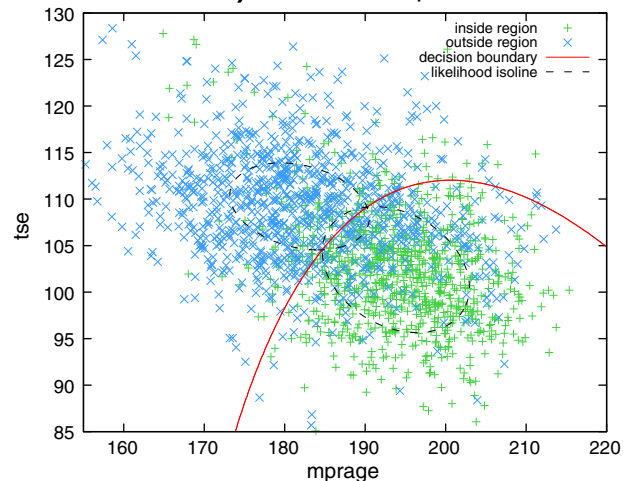


Fig. 6. This figure shows in (A) the final estimate of the PAC region as the green labeled surface patch together with the deformed contour of the inner sampling region due to the initial atlas label in black for the same data set used in Figs. 3, 4. Notice the increase in hyper-intensities within the PAC estimate compared with the initial likelihood mapping in Fig. 4B. Panel (B) shows the feature space after optimization of the distributional estimates and induced classifier. The underlying MR feature distributions are optimally separable compared with the two clusters in Fig. 5.

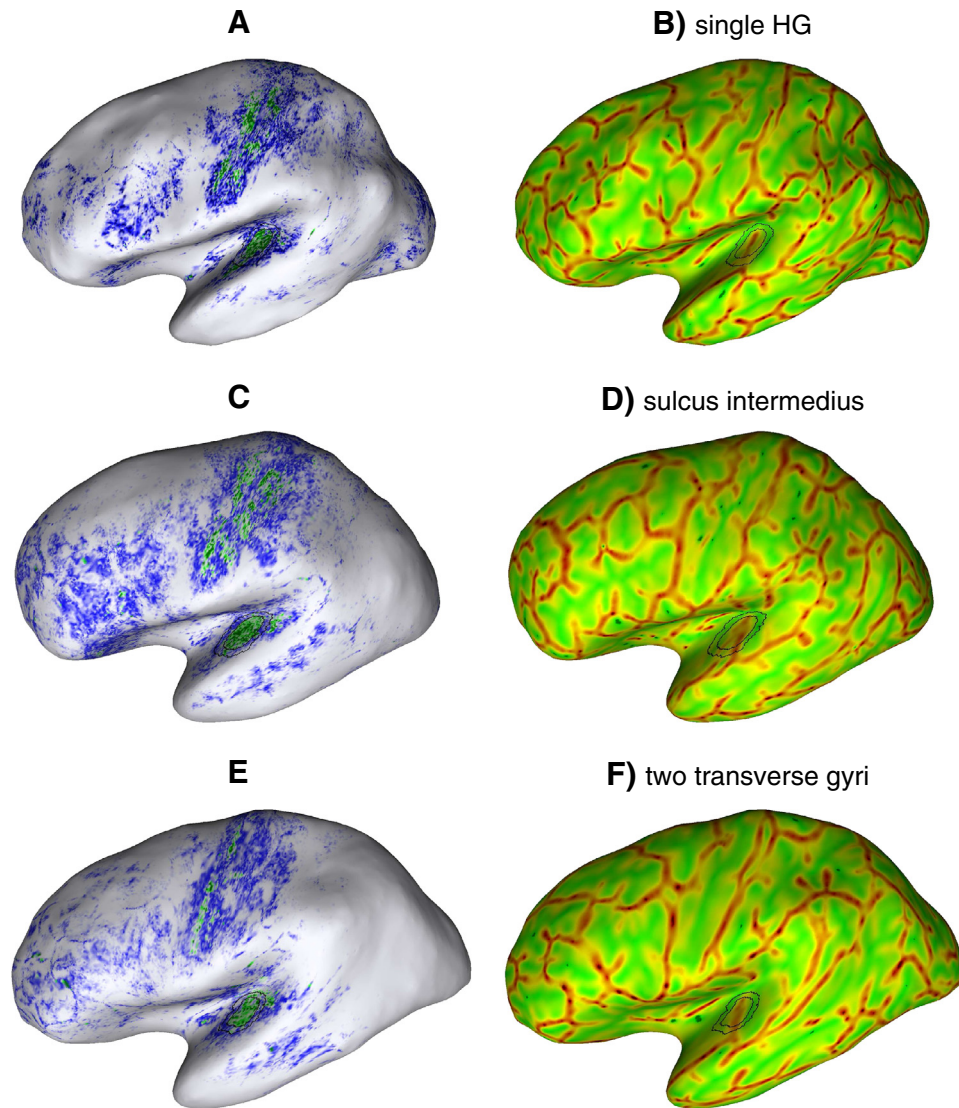


Fig. 7. Examples of individual mapping results due to our approach for in-vivo localization of the human PAC area. Each row shows the likelihood map (left) and curvature overlay (right) for one of our subjects. The final sampling regions are drawn in each map for anatomical orientation. Here, we selected subjects with a different temporal cortex anatomy in the left hemispheres: Heschl's gyrus with (second row) and without sulcus intermedius (top and bottom) and one subject with an additional transverse temporal gyrus (bottom row). A higher myelinated region (green labeling) of plausible size can be identified on the medial two thirds of Heschl's gyrus in each hemisphere (cf. Shape, anatomical location and spatial extent of the PAC estimate section).

498 proposed local approach can be expected to fail in cases where the
 499 underlying assumption does not hold that the inner sampling region R_{in}
 500 overlaps the highly myelinated PAC to a higher degree than the region
 501 R_{out} . Due to the inherent limitations of image registration techniques
 502 to precisely map brain regions of high anatomical variability, the initial,
 503 atlas-based estimate of the inner sampling regions in the individual
 504 brains may or may not properly cover Heschl's gyrus, and the contained
 505 PAC area, respectively. The robustness of our method to initialization
 506 error has been shown by comparing the estimated parameters of the
 507 joint distribution of likelihood values over the entire hemispheres due
 508 to the automatic, atlas-based initialization of R_{in} (case 1) and selectively
 509 introduced initialization error (cases 2 and 3). For the case study 2, the
 510 over- and underestimation of the shape and location of HG have been
 511 simulated by largely perturbing the parameter values $w_m, m = 0$, of
 512 the automatically estimated ellipsoid embedding. More precisely, we let

$$\vec{v} \in \{ \vec{v} : \vec{v} \text{ within } 1 \text{ cm distance to } \vec{c} \},$$

$$R \in \{ R_x(\phi), R_y(\phi), R_z(\phi) \} \text{ and } \phi \in \{ 20^\circ, -20^\circ \},$$

$$d \in \{ 0.5, 1.5 \}.$$

513

For case study 3, we selected subjects with multiple transverse tem- 515
 516 poral gyri and systematically mis-initialized R_{in} on the second transverse
 517 temporal gyrus. We also initialized R_{in} within the motor cortex region of
 518 single subjects and compared the different mapping results.

519 Further, the results due to the Gaussian weighing of the raw MR intensities
 520 have been compared with that due to an experimentally defined optimal
 521 kernel.

522 The anatomical information provided by the curvature overlays
 523 (see, e.g., Fig. 7) helps neuroscientists to identify hyper-intense patches
 524 (i.e., compact cortex regions with high likelihood-difference values) in
 525 the temporal region of each individual hemisphere and to compare
 526 the location and extent of these regions with anatomic definitions of
 527 the human auditory cortex due to Brodmann (1909), Morosan et al.
 528 (2001), von Economo and Horn (1930).

529 In addition to the surface overlays we used volumetric representa-
 530 tions of the resulting maps in the form of gray matter ribbons (Fig. 11).
 531 These ribbons have been initialized as empty matrices that are registered
 532 with the underlying MR data sets and have the same spatial resolution. 532 Q8
 533 The positive likelihood-difference values have then been projected
 534 from the vertices back to voxels between the individual anatomical

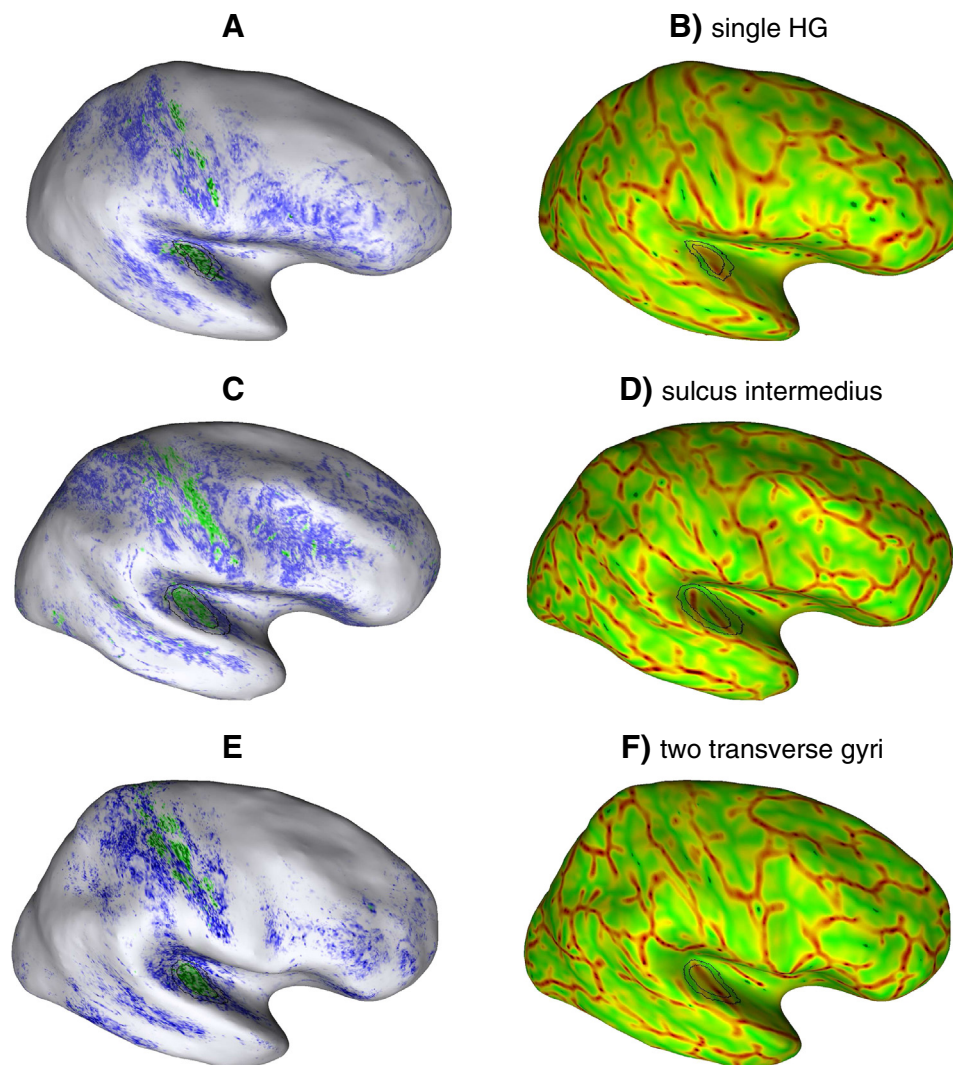


Fig. 8. Additional examples of individual mapping results due to our approach for in-vivo localization of the human PAC area. Here, we selected further subjects with a different temporal cortex anatomy in the right hemispheres: Heschl's gyrus with (second row) and without sulcus intermedius (top and bottom) and one subject with an additional transverse temporal gyrus (bottom row). A higher myelinated region (green labeling) of plausible size can be identified on the medial two thirds of Heschl's gyrus in each case (cf. Shape, anatomical location and spatial extent of the PAC estimate section).

535 surfaces, such that locally maximum intensities in the ribbons indicate
 536 the PAC region and possibly further areas with similar tissue properties
 537 (middle column in Fig. 11). The superimposed pial surfaces and gray–
 538 white matter boundaries (blue and red contours in Fig. 11) provide ana-
 539 tomical information and support the visual inspection of the results.
 540 These individual 3D representations have been used for the analysis of
 541 possible misclassifications due to partial volume effects and artifactual
 542 intensity fluctuations present in the MR data, as well as pre-processing
 543 and mapping errors.

544 Evaluation of the PAC estimate

545 In combination with the anatomical information provided by the
 546 MPRAGE volumes, the gray matter ribbons have been used to compare
 547 the location, shape and extent of the individual PAC estimates with ana-
 548 tomic definitions of the human PAC according to Brodmann (1909),
 549 Morosan et al. (2001), von Economo and Horn (1930).

550 Since our algorithm does not employ smoothness constraints, it does
 551 not necessarily provide accurate segmentations of the cortex regions of
 552 interest. The chosen constraints rather imply a classification of the MR
 553 features, from which a segmentation of the PAC regions could be derived
 554 in a further step. For example, the contour shown in Fig. 6A has been

drawn after convergence based on the parametrization of the optimal
 555 sampling region R_{in} . It indicates the location of the PAC estimate in one
 556 of our subjects, but does not represent the PAC area boundary. In this
 557 case, the optimal, elliptic sampling region underestimates the PAC area,
 558 and does not completely cover the hyper-intense surface patch that can
 559 be considered as the PAC. While being relatively straightforward for a
 560 neuroscientist to outline the corresponding surface region based on the
 561 color-coded overlay and anatomical knowledge, the automatic segmen-
 562 tation must be seen as an ill-posed, inverse problem. This is due to the
 563 fact that the solution does not continuously depend on the data (as
 564 both, the raw input data and the final in-vivo maps provide noisy and
 565 incomplete information), while the problem may have multiple possible
 566 solutions (because the shape and spatial extent of the PAC area may
 567 vary dramatically across subjects and hemispheres). These difficulties
 568 can be alleviated by imposing additional constraints – in the form of vari-
 569 ational principles or information about the statistical properties of the
 570 solution space (e.g., a model of the human PAC shape variation) – into
 571 an adequate segmentation algorithm, which will be subject to future
 572 work. Hence, the surface overlays were used here in combination with
 573 the location of the final contours to manually inspect the underlying
 574 hyper-intense regions within the temporal lobes (green color in Figs. 7
 575 to 10) w.r.t. their spatial extent and homogeneity. 576

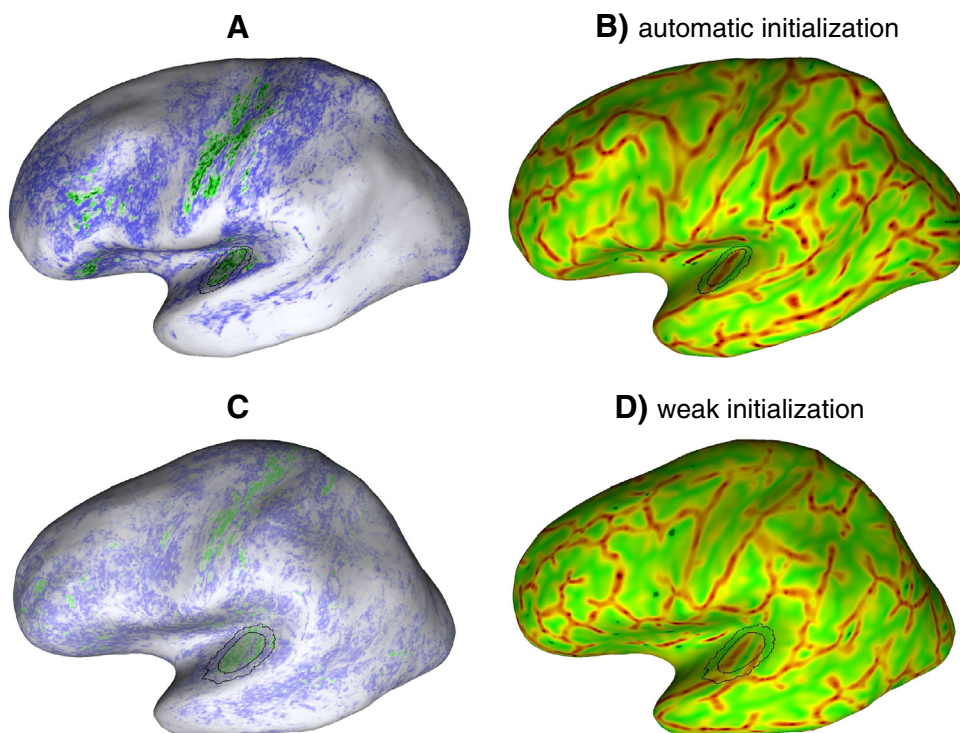


Fig. 9. This figure compares mapping results due to the automatic (top row) and weak initializations (bottom) of the sampling regions. As discussed in the Robustness of the classification algorithm section, the mis-initialization of the inner sampling region over the second transverse temporal gyrus (bottom row) affects the discriminatory power of the classifier. In these cases the PAC region tends to be overestimated in individual subjects, and the overall likelihood-difference (i.e., intensity of the labelings) tends to decrease.

Further, group average maps have been computed over the left and right hemispheres and directly compared with the maximum probability maps of the PAC due to Morosan et al. (2001) (see Fig. 13). Therefore, the surfaces have been aligned across individuals using spherical registration (Fischl et al., 1999b) with the anatomical information present in FreeSurfer's "fsaverage" template and then the individual likelihood of increased myelination has been averaged at each surface node. Areas in the population average map were finally identified by comparisons with the probabilistic cytoarchitectonic areas of interest that have been independently mapped to the FreeSurfer template. In order to generate the surface label for region Te1 the volume-based maximum probability map of each post-mortem subject provided by Morosan et al. (2001) has been mapped to a surface reconstruction of the subject's cortical hemispheres. These surfaces have then been brought into the register as described above and the individual surface labels were mapped to the "fsaverage" surface using a vertex-wise logical disjunction. As a result, the red contour in Fig. 13 encloses the maximum extent of region Te1 in the surface-based maximum probability maps of Te1.

Results

In our study, the algorithm always converged after 10 to 25 iterations and identified a higher myelinated region of plausible size on the medial two thirds of Heschl's gyrus in each of the 78 hemispheres. Representative examples are provided in Figs. 7 and 8. The optimization strategy with default parametrization boosted effects of differences in the tissue-specific MR properties between the primary and secondary auditory cortex areas.

Robustness of the classification algorithm

We found evidence that the presented analysis is robust to initialization. The over-simplified shape constraint in combination with a lower bound on the sampling region size effectively prevented trivial solutions (i.e., the inside region did not converge into a single point or became too

large to allow correct classifications) without imposing a strong bias on the individual shape and size of the PAC estimates. The atlas-based approach produced sufficiently accurate and robust initializations, from which the final estimates identified a higher myelinated region of plausible size on the medial two thirds of Heschl's gyrus in all hemispheres under study (see Shape, anatomical location and spatial extent of the PAC estimate section).

Another strong hint for the robustness of the method to initialization is provided by the observed regions that indicate primary cortex areas beyond the PAC (see Shape, anatomical location and spatial extent of the PAC estimate section).

Furthermore, the Gaussian weighting of MR intensities along the normal profiles provided a good approximation of the weighting that optimized the separability of the distributions induced by the initial classifier (see Fig. 12A).

Optimization of the Jensen–Shannon divergence (Eq. (2)) resulted in fitting the inside region to a cortex region with positive likelihood-difference, and hence higher myelination. Fig. 12B shows that the algorithm always converged after 10 to 25 iterations and produced comparable results for further possible choices for the objective function. That is, optimizing the Jensen–Shannon divergence optimized other criteria as well. There were, however, advantages of the chosen criterion, most importantly that the Jensen–Shannon divergence encouraged reasonably small regions and ensured convergence of the gradient ascent implementation. Local classification errors, as further discussed below, did not appear in the group average map in Fig. 13, and could be attributed to sampling error rather than ill-posed optimization criteria.

The myelin maps were robust to the precision of the automatic initializations (case 1). However, as expected, the local approach failed in cases where the inner sampling region R_{in} did not overlap the highly myelinated PAC to a higher degree than the region R_{out} . We observed no significant difference (i.e., $p > 0.2$, paired t -tests) in the parameters of the joint distribution of likelihood values in the resulting surface overlays when comparing the automatic (case 1) and weakened (case 2) initial estimates. However, the results differ significantly when reducing the

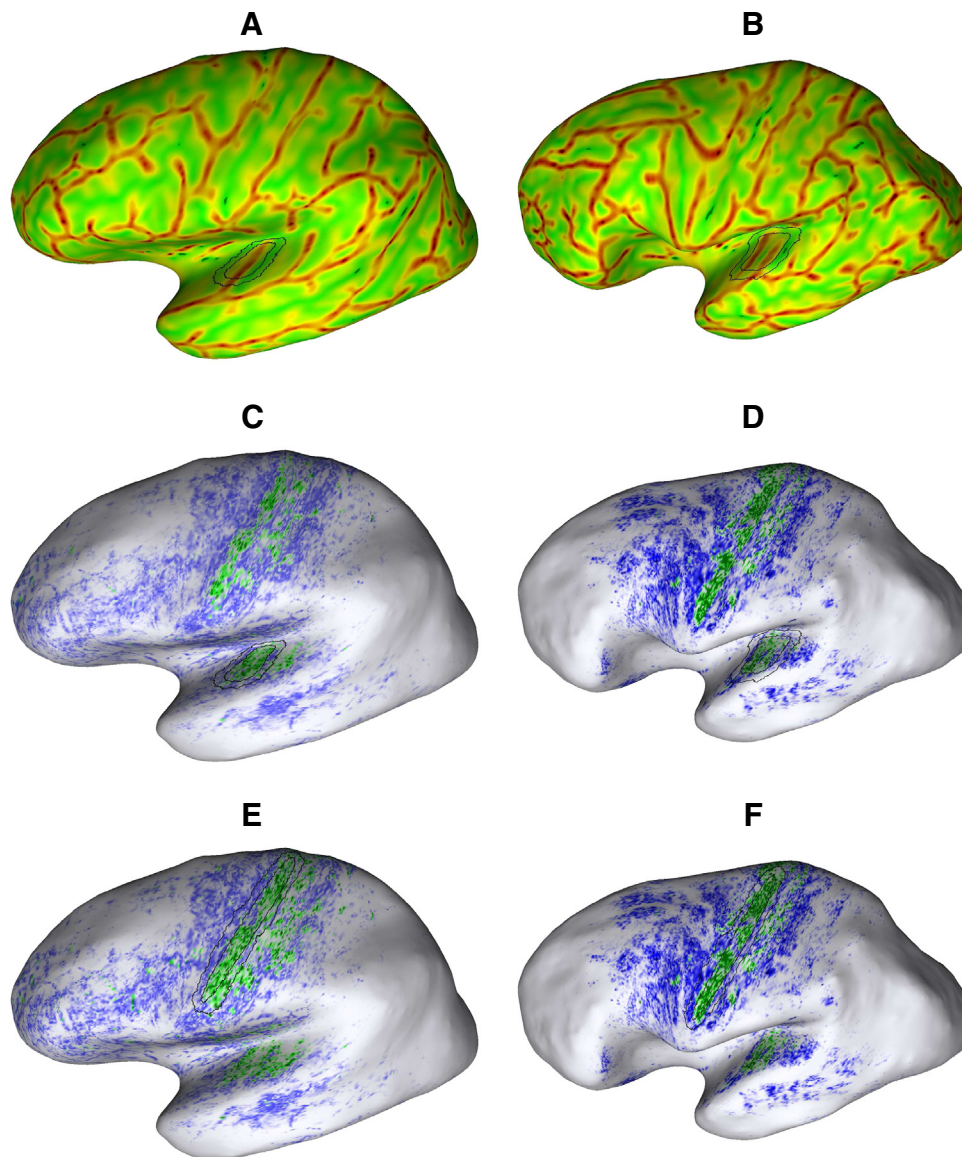


Fig. 10. Mapping results due to the automatic initialization (middle row) of the sampling regions and the initialization in the motor cortex area (bottom row) for two subjects. The black contours in panels e and f represent the primary motor cortex in terms of a probability map of BA 4p taken from the FreeSurfer atlas at the threshold of $p > 0.1$ (FST). In both hemispheres and cases, the regions of hyper-intense green labeling within the temporal cortex represent anatomically correct in-vivo estimates of the individual PAC area. Notice that the overall likelihood patterns were largely unaffected, i.e., the discriminatory power of the statistical classifier was comparable in both cases of initialization. This demonstrates the robustness of our method to atlas-based initialization.

643 histogram analysis from the entire cortical hemispheres to the temporal
 644 lobes only. In particular, a mis-initialization of the inner sampling region
 645 on the second transverse temporal gyrus, if present, yielded misclassifications.
 646 As visible in Fig. 9, in these cases the PAC region tends to be
 647 overestimated in individual subjects, while the overall likelihood-
 648 difference and the discriminatory power of the classifier tends to de-
 649 crease. This effect is indicated by the less intense labeling in Fig. 9C com-
 650 pared with Fig. 9A. An exception was observed in case study 3: We found
 651 no striking impact of the initializations in the motor cortex on the shape
 652 and location of the individual PAC estimates (see Fig. 10). This clearly in-
 653 dicates the robustness of the method to initialization given that the inner
 654 sampling region R_{in} overlaps a region with tissue properties that are sim-
 655 ilar to those of the highly myelinated PAC.

656 Shape, anatomical location and spatial extent of the PAC estimate

657 The group result given in Fig. 13 shows that the average location of
 658 the PAC area as defined by our method in vivo (the intense green pat-
 659 tern in Fig. 13) is well within the maximum probability location of the

primary auditory cortex (red line in Fig. 13) as defined in post- 660
 mortem brains by Morosan et al. (2001). The regularity of the pattern 661
 even indicates that our method provides a more compact definition of 662
 the PAC region across subjects compared with the surface-based repre- 663
 sentation of area Te1. More precisely, the location of strongest labeling 664
 with a more medial geometric center compared to the maximum prob- 665
 ability map for Te1 may suggest a better correspondence to areas Te1.1 666
 and Te1.0. However, this observation needs further investigation. Also, 667
 it must be noted that the maximum probability map of the PAC region 668
 is originally defined in post-mortem volume data and had to be brought 669
 into the register with the template surface shown in Fig. 13. Observed 670
 differences in the shape of the in vivo and post-mortem estimates of 671
 the PAC area may be attributable to registration error. 672

A second auditory area of less intense labeling was observed in the 673
 group map posterior to the medial part of Heschl's gyrus outside the 674
 probability map for primary auditory cortex. 675

We did not repeatedly observe hyper-intense patches on planum 676
 polare such as identified in the R1-maps by Sigalovsky et al. (2006). 677
 The single observations were canceled out in the group map. 678

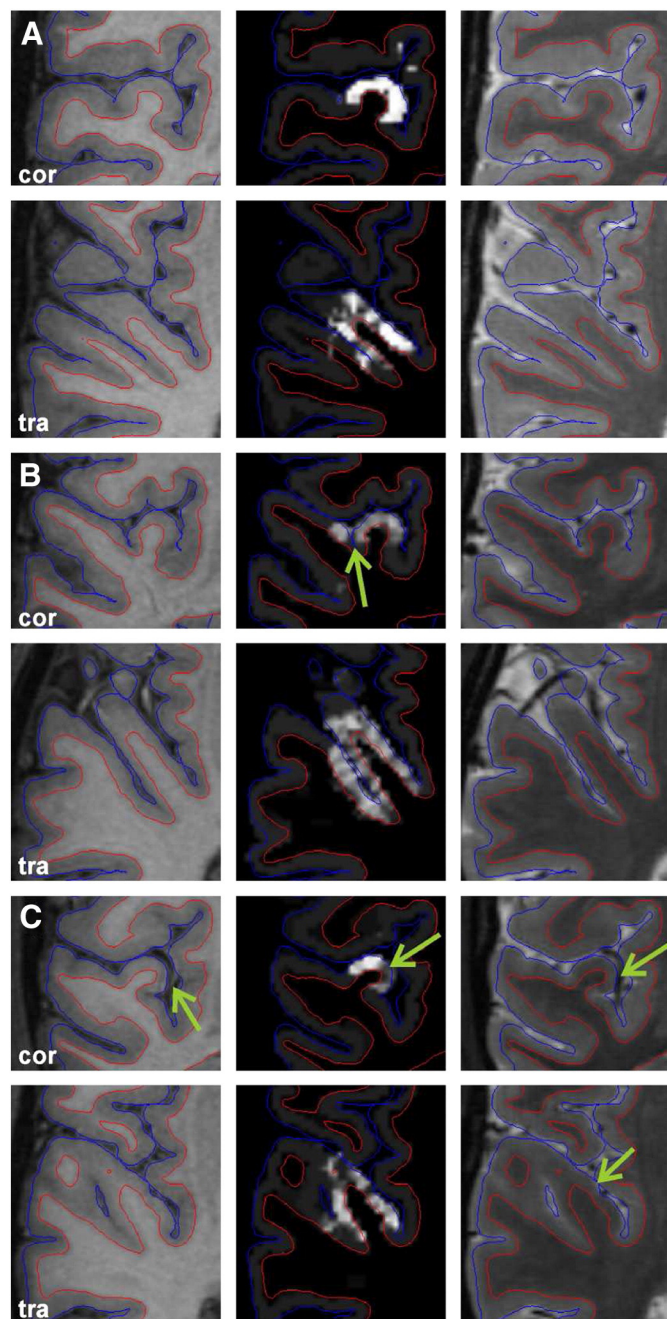


Fig. 11. Auditory cortex area of three individual brains (A, B, C) in coronal and transversal views. The middle column shows the cortical area with high likelihood-difference values. The corresponding T1 weighted and T2 weighted images are shown in the left and right columns, respectively. The red and blue contours indicate the location of the inner and outer cortical boundary, respectively. The arrows point to erroneous classification results which are due to segmentation errors (B) or artifacts in the anatomical data due to large blood vessels (C).

fitting “neither” known local distribution (indicated by the white labeling in Fig. 13).

On a single subject level, visual inspection of the results showed that a region on the medial two thirds of Heschl's gyrus was labeled in each subject and hemisphere (see Figs. 7, 8 and 11 for examples of in vivo maps of single subjects with a different temporal cortex anatomy). This area can be identified in each of the individual brains under study with a similar precision compared to the population-average map.

However, depending on the signal to noise ratio of the anatomical data, which mainly depends on the subjects head motion during the anatomical scans, the likelihood-difference values can vary (compare Figs. 11A and B). Furthermore, misclassifications could be observed that are due to artifacts in the MR, such as the artifacts produced by blood flow within large vessels (Fig. 11C). We also observed errors in segmentation especially in deep sulci that introduce large bias to the classification result, and alter the homogeneity and shape of the estimated cortex regions.

Discussion

The results of our study show that the proposed local, data-driven approach is able to boost the effects of the differences in the measured tissue properties between the PAC and secondary auditory cortex. These differences are mainly due to higher myelin content within the lower layers of primary cortical areas that have been adequately emphasized by the definition of the profile lines and Gaussian weighting (Fig. 2). The primary auditory cortex area due to the statistical classifier could be identified in all individual subjects with a similar precision compared to the population-average map and is in close correspondence with anatomic definitions of the PAC.

We are fully aware of the problem that there is currently no gold standard of defining the PAC in vivo. Therefore any firm conclusion on the power of in vivo architectonic methods in general and ours in particular must await future progress in tonotopic mapping and/or combined in vivo and subsequent post-mortem studies (e.g., Seewann et al., 2012) on the same subjects. However, a comparison with the current state of the art, i.e., the probabilistic maps provided by Morosan et al. (2001) suggests the feasibility of our approach. Its full potential must, however, be refined in future studies (see below).

A second argument on the feasibility of our approach is that it elucidated a second auditory area with high myelin content located posterior to the medial part of Heschl's gyrus. Its location is outside the probability map for primary auditory cortex as defined by cytoarchitecture (Morosan et al., 2001), but may be consistent to the medial part of area ttrll described by Beck (1930) as an area that is most similar to the primary areas w.r.t. myelin content. Wallace et al. (2002) described an area PA with a similar location and also stated that the myelin staining profile was similar to that of the PAC area. A similar auditory area was also observed in some subjects of a tonotopic fMRI study by Formisano et al. (2003) and more recently by Dick et al. (2012) using functional and myeloarchitectonic mapping. This second auditory area has not been described by Sigalovsky et al. (2006) possibly due to lower resolution and/or field strength. Also the study of Glasser and Van Essen (2011) did not resolve this additional area possibly due to the whole brain approach and compensation of MR intensity variations (by bias field and outlier removal, re-sampling and smoothing). The benefit to be gained from the combination of $d \geq 1$ MR contrasts to reduce the labeling of non-PAC areas on planum temporale thus needs further investigation.

Our method further generated feasible labelings in the group map along the pre- and post-central gyri, corresponding to the strongly myelinated primary motor cortex and somatosensory cortex, which is also a primary region. These results demonstrate the validity and robustness of our method, since our classifier was optimized for the localization of the auditory cortex region.

The green pattern enclosed by the black contour in Fig. 13 indicates that the primary motor cortex can be identified in the group map.

In addition to the primary auditory and motor cortex regions, we further observed less intense patches of labeling within the location of the somatosensory cortex posterior to the motor cortex. In direct comparison with the results presented by Dick et al. (2012), Glasser and Van Essen (2011) and anatomic definitions of the primary motor and somatosensory cortices (e.g., Brodmann, 1909), these estimates were less reliable.

The primary visual cortex was not apparent in the group result. Our algorithm classified the MR feature values within the visual cortex as

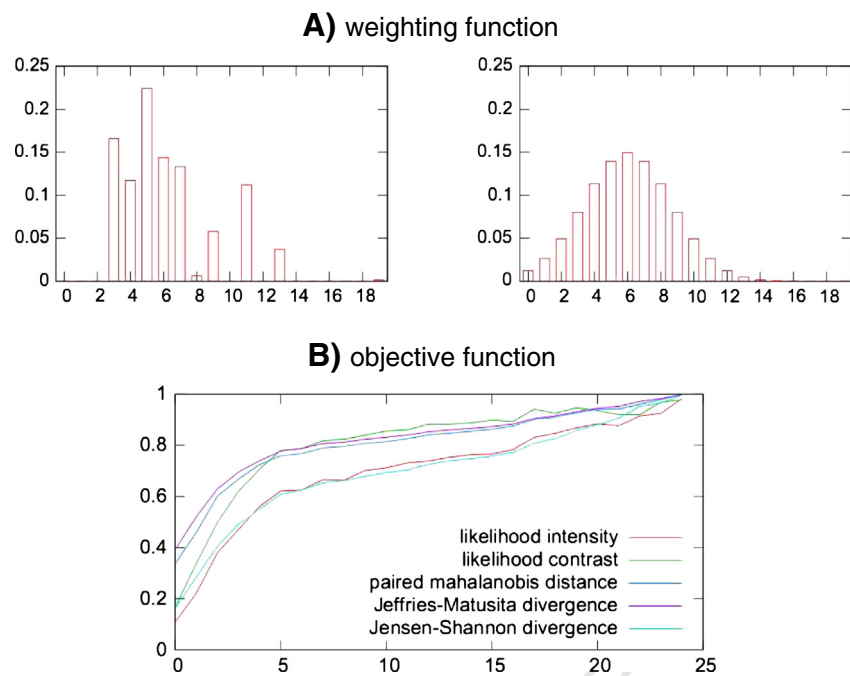


Fig. 12. Evaluation of the robustness of the algorithm: panel (A) indicates that the experimentally defined optimal weighting (left) can be approximated by a Gaussian kernel (right) that is centered and scaled such that MR values sampled from the lower layers of the gray matter are emphasized. Panel (B) shows the experimental behavior of the Jensen–Shannon divergence (light blue curve) and other possible choices for the objective function during optimization (here, over 23 iterations).

753 However, the primary motor and somatosensory cortices have been
 754 more clearly revealed by recent global approaches that are based on al-
 755 ternative concepts for myelin mapping, for example (Dick et al., 2012;
 756 Glasser and Van Essen, 2011). Reduction of the MR signal inhomogene-
 757 ities due to different sensitivities of the MR coil elements could probably
 758 delineate these regions more clearly in future studies. We are convinced
 759 that methods will be developed that produce more homogeneous data
 760 than we used in this study. Moreover, we think that with homogeneous
 761 data our method would work without the atlas-based initialization step.
 762 The impact of field inhomogeneities and the bias due to (local) curva-
 763 ture and anatomical labeling nonetheless need further investigation.

764 The primary visual cortex was not apparent in the group result, pre-
 765 sumably due to larger intensity variations and partial volume effects in
 766 this cortex region. It is well known that automatic segmentation does
 767 not reliably extract the primary visual cortex due to the comparatively
 768 small cortical thickness. It is common practice to manually refine auto-
 769 mated segmentations and correctly identify the pial surface and gray-
 770 white matter boundary (e.g., Schira et al., 2009). The result of our
 771 study suggests that the unsupervised, local approach does not account
 772 for such variations in the measured tissue properties and for possible
 773 sampling error due to sub-optimal pre-processing.

774 We found evidence that our method is robust to the chosen con-
 775 straints on the sampling and optimization parameters. The data-
 776 driven approach is however sensitive to the signal to noise ratio of
 777 the anatomical data that mainly depends on the subjects' head mo-
 778 tion and spatial resolution of the MR measurements. Partial volume
 779 effects and possible artifacts in the MR data (e.g., due to blood flow
 780 within large vessels) caused misclassifications. Although these mis-
 781 classifications were rather small in size, this is a serious problem
 782 that can only be solved in an automatic way if the data are acquired
 783 at a higher spatial resolution. Unfortunately, this is not feasible due
 784 to too long scan time and head motion. However, averaging repeated
 785 scans of single subjects acquired in several sessions and using, e.g., a
 786 32 channel coil instead of only 8 channels as done here could im-
 787 prove the signal to noise ratio and thus the precision of the localiza-
 788 tion of PAC in individual brains.

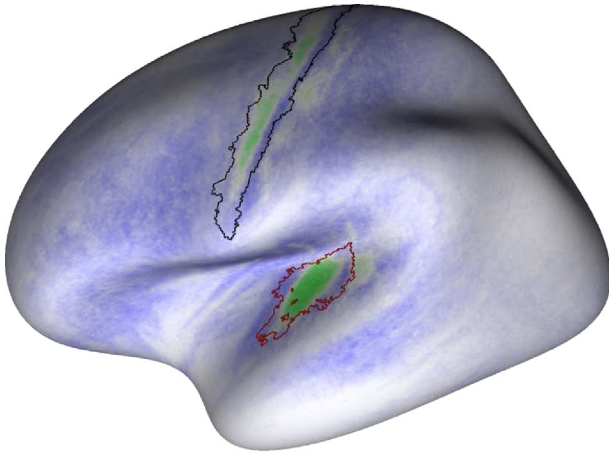
Conclusion

789 We presented a fully automatic method that was shown to be able to
 790 define the human primary auditory cortex area in vivo. A statistical clas-
 791 sifier was applied to a combination of anatomical MR intensities to com-
 792 pute individual maps of regional differences in the myelin content in
 793 cortical gray matter. The primary auditory cortex area due to the classi-
 794 fier could be identified in individual subjects with a similar precision
 795 compared to the population-average map and exhibited a close corre-
 796 spondence with anatomic definitions of the PAC.

797 In contrast to previous work, our method is based on a standard atlas
 798 for observer-independent initialization and simple prior models of cor-
 799 tex anatomy and regional myelin content homogeneity. Most notably,
 800 our results showed that the PAC area can be estimated without
 801 resorting to re-sampling and surface-based smoothing of the data, as
 802 well as removal of artifacts and outliers in the raw data. This largely
 803 avoids bias at the cost of obtaining neither necessarily smooth segmen-
 804 tations of the PAC, nor a complete, detailed parcellation of the entire
 805 cortices of individuals. However, the method may be improved towards
 806 smooth area delineation by adapting more sophisticated, global opti-
 807 mization schemes, e.g., combinatorial approaches such as graph cuts
 808 (Rohkohl and Engel, 2007), for template-free simultaneous classifica-
 809 tion and estimation under spatial smoothness constraints.

810 As this method is based on conventional anatomical MR images, the
 811 necessary data can be acquired on a routine basis. Thus, the primary au-
 812 ditory and also motor cortex areas could be extracted from the data of
 813 exactly those subjects who participated in an MR experiment and be
 814 used as specific templates for fMRI data analysis. Future validations
 815 must determine whether such an approach is more precise than using
 816 probability maps defined in post-mortem data (e.g., Fischl et al., 2008;
 817 Tahmasebi et al., 2009). To use this method for single subject deline-
 818 ation of the PAC area from neighboring secondary cortex, the data must
 819 be improved, e.g., by minimizing head motion and/or averaging across
 820 repeated scans, by correcting for global intensity variations during
 821 data acquisition, by eliminating small artifacts produced by blood ves-
 822 sels and by improving automatic cortex segmentation. In particular
 823

A) left hemisphere average



B) right hemisphere average

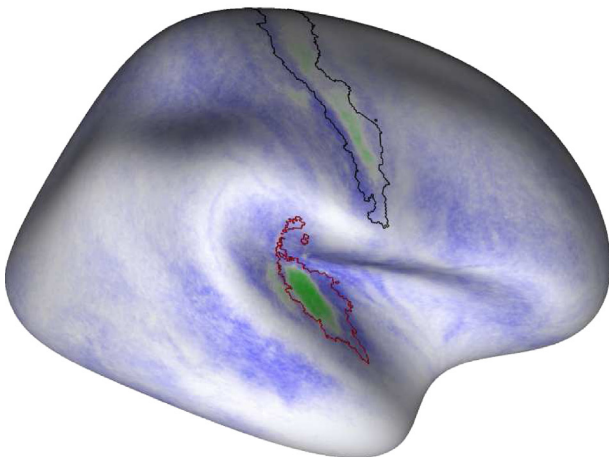


Fig. 13. Likelihood-difference maps averaged across all 39 subjects. Green areas indicate population average regions with higher myelin content. The region of hyperintense green labeling within the temporal cortex is our probabilistic in-vivo estimate of the PAC area. The red line represents the maximum probability for the boundary of area Te1, i.e., the PAC area as defined in post-mortem brains (Morosan et al., 2001) and projected onto the template surface. The black contour represents the primary motor cortex in terms of a probability map of BA 4p taken from FreeSurfer at $p > 0.1$ (FST).

precise segmentations of the gray matter would provide the necessary prerequisite for several model-based improvements and possible fine-tuning of the in-vivo maps: It is for example known that the myelin content varies with curvature and cortical thickness, and the measured MR intensities may be adjusted to compensate for this effect (e.g., Sereno et al., 2012). A more sophisticated sampling of the MR volumes in radial distance or a curvature-dependent weighting of the samples may then much better account for regional differences in the “true” columnar organization and compression of the lower cortex layers (as apparent in Fig. 1A) and reveal much smoother and more clearly separable PAC areas in the individual maps.

To further increase the quality of the results, it may be beneficial to utilize ultra-high field MRI (Cohen-Adad et al., 2012; Duyn, 2012a) and/or other MR contrasts, e.g., proton density, magnetization transfer, or susceptibility weighted imaging (Duyn, 2012b) to exploit additional complementary tissue information that more clearly reveal the myeloarchitectonic differences between the multiple human cortex areas. Finally, the results in single subjects must be compared to other means of defining the primary auditory cortex, i.e., by tonotopic mapping experiments using high resolution fMRI.

We think that the proposed classification approach supports a multi-modal approach of joint functional detection and estimation of specific brain regions in vivo. In contrast to previous work, inclusion of further MR scans as well as functional activation maps (and possibly data from other modalities at different resolutions) is straightforward. Adding data sets would simply alter the dimensions d of the feature space. Our approach further supports the quantitative evaluation of the benefit to be gained from additional experimental data. Moreover, it preserves the spatial resolution and specificity of current MRI by largely avoiding the unquantifiable bias possible due to re-sampling, correction and smoothing of the raw data. This is essential for the robust localization and precise delineation of the human PAC areas, and even more so of higher-order functional fields.

Acknowledgment

The authors would like to thank Katrin Amunts and Patricia Morosan for providing the probability maps of Te1 and Te2 and Monika Dobrowolny for data acquisition. The work was supported by the BMBF grant “Prosody and Song” (FKZ: 01GW0621) and the DFG SFB-TRR 31 “Active Listening”.

References

- Bar-Hillel, A., Spiro, A., Stark, E., 2006. Spike sorting: Bayesian clustering of non-stationary data. *J. Neurosci. Methods* 1570 (2), 303–316.
- Beck, E., 1930. Die Myeloarchitektonik der dorsalen Schläfenlappenrinde beim Menschen. *J. Psychol. Neurol.* 41, 129–263.
- Bridge, H., Clare, S., Jenkinson, M., Jezzard, P., Parker, A.J., Matthews, P.M., 2005. Independent anatomical and functional measures of the V1/V2 boundary in human visual cortex. *J. Vis.* 50 (2), 93–102 (ISSN 1534-7362).
- Brodman, K., 1909. Vergleichende Lokalisationslehre der Großhirnrinde. Johann Ambrosius Barth, Leipzig.
- Clarke, S., Rivier, F., 1998. Compartments within human primary auditory cortex: evidence from cytochrome oxidase and acetylcholinesterase staining. *Eur. J. Neurosci.* 100 (2), 741–745.
- Cohen-Adad, J., Polimeni, J.R., Helmer, K.G., Benner, T., McNab, J.A., Wald, L.L., Rosen, B.R., Mainiero, C., 2012. T2* mapping and b0 orientation-dependence at 7 T reveal cyto- and myeloarchitectonic organization of the human cortex. *NeuroImage* 600 (2), 1006–1014.
- Da Costa, S., van der Zwaag, W., Marques, J.P., Frackowiak, R.S.J., Clarke, S., Saenz, M., 2011. Human primary auditory cortex follows the shape of Heschl’s gyrus. *J. Neurosci.* 310 (40), 14067–14075.
- Dale, A.M., Fischl, B., Sereno, M.I., 1999. Cortical surface-based analysis 1. Segmentation and surface reconstruction. *NeuroImage* 90 (2), 179–194.
- Desikan, R.S., Ségonne, F., Fischl, B., Quinn, B.T., Blacker, D., Dickerson, B.C., Buckner, R.L., Dale, A.M., Maguire, R.P., Hyman, B.T., Albert, M.S., Killiany, R.J., 2006. An automated labeling system for subdividing the human cerebral cortex on MRI scans into gyral based regions of interest. *NeuroImage* 310 (3), 968–980.
- Dick, F., Tierney, A.T., Lutti, A., Josephs, O., Sereno, M.I., Weiskopf, N., 2012. In vivo functional and myeloarchitectonic mapping of human primary auditory areas. *J. Neurosci.* 32, 16095–16105.
- Duyn, J.H., 2012a. The future of ultra-high field MRI and fMRI for study of the human brain. *NeuroImage* 620 (2), 1241–1248.
- Duyn, J.H., 2012b. MR susceptibility imaging. *J. Magn. Reson.*
- Duyn, J.H., van Gelderen, P., Li, T.Q., de Zwart, J.A., Koretsky, A.P., Fukunaga, M., 2007. High-field MRI of brain cortical substructure based on signal phase. *Proc. Natl. Acad. Sci. U.S.A.* 104, 11796–11801.
- Eickhoff, S., Walters, N.B., Schleicher, A., Kril, J., Egan, G.F., Zilles, K., Watson, J.D., Amunts, K., 2005. High-resolution MRI reflects myeloarchitecture and cytoarchitecture of human cerebral cortex. *Hum. Brain Mapp.* 24, 206–215.
- Fischl, B., Dale, A.M., 2000. Measuring the thickness of the human cerebral cortex from magnetic resonance images. *Proc. Natl. Acad. Sci. U.S.A.* 970 (20), 11050.
- Fischl, B., Sereno, M.I., Dale, A.M., 1999a. Cortical surface-based analysis 2. Inflation, flattening, and a surface-based coordinate system. *NeuroImage* 90 (2), 195–207.
- Fischl, B., Sereno, M.I., Tootell, R.B.H., Dale, A.M., 1999b. High-resolution intersubject averaging and a coordinate system for the cortical surface. *Hum. Brain Mapp.* 80 (4), 272–284.
- Fischl, B., Liu, A., Dale, A.M., 2001. Automated manifold surgery: constructing geometrical-ly accurate and topologically correct models of the human cerebral cortex. *IEEE Trans. Med. Imaging* 200 (1), 70–80.
- Fischl, B., Van Der Kouwe, A., Destrieux, C., Halgren, E., Segonne, F., Salat, D.H., Busa, E., Seidman, L.J., Goldstein, J., Kennedy, D., 2004. Automatically parcellating the human cerebral cortex. *Cereb. Cortex* 140 (1), 11.
- Fischl, B., Rajendran, N., Busa, E., Augustinack, J., Hinds, O., Yeo, B.T., Mohlberg, H., Amunts, K., Zilles, K., 2008. Cortical folding patterns and predicting cytoarchitecture. *Cereb. Cortex* 180 (8), 1973–1980.
- Flechsig, P., 1908. Bemerkungen über die Hörsphäre des menschlichen Gehirns. *Neurol. Zentrabl.* 27 (2–7), 50–57.

- 918 Formisano, E., Kim, D.S., Di Salle, F., van de Moortele, P.F., Ugurbil, K., Goebel, R., 2003. Mirror-
919 symmetric tonotopic maps in human primary auditory cortex. *Neuron* 40, 859–869.
- 920 FST, T. The FreeSurfer toolkit (and Brodmann area labels) [http://surfer.nmr.mgh.harvard.](http://surfer.nmr.mgh.harvard.edu/)
921 [edu/](http://surfer.nmr.mgh.harvard.edu/).
- 922 Galaburda, A., Sanides, F., 1980. Cytoarchitectonic organization of the human auditory
923 cortex. *J. Comp. Neurol.* 190, 597–610.
- 924 Glasser, M.F., Van Essen, D.C., 2011. Mapping human cortical areas in vivo based on
925 myelin content as revealed by T1- and T2-weighted MRI. *J. Neurosci.* 310 (32),
926 11597–11616.
- 927 Hackett, T.A., Preuss, T.M., Kaas, J.H., 2001. Architectonic identification of the core region in
928 auditory cortex of macaques, chimpanzees, and humans. *J. Comp. Neurol.* 4410 (3),
929 197–222.
- 930 Hinds, O., Polimeni, J.R., Rajendran, N., Balasubramanian, M., Wald, L.L., Augustinack, J.C.,
931 Wiggins, G., Rosas, H.D., Fischl, B., Schwartz, E.L., 2008. The intrinsic shape of
932 human and macaque primary visual cortex. *Cereb. Cortex* 180 (11), 2586–2595.
- 933 Hopf, A., 1954a. Die Myeloarchitektonik des Isocortex temporalis beim Menschen.
934 *J. Hirnforsch.* 1, 208–279.
- 935 Hopf, A., 1954b. Zur Frage der Konstanz und Abgrenzbarkeit myeloarchitektonischer
936 Rindenfelder. *J. Neurol.* 1720 (2), 188–200.
- 937 Humphries, C., Liebenthal, E., Binder, J.R., 2010. Tonotopic organization of human auditory
938 cortex. *NeuroImage* 50, 1202–1211.
- 939 Kaas, J.H., Hackett, T.A., 1998. Subdivisions of auditory cortex and levels of processing in
940 primates. *Audiol. Neuro Otol.* 3, 73–85.
- 941 Langers, D.R., Backes, W.H., van Dijk, P., 2007. Representation of lateralization and
942 tonotopy in primary versus secondary human auditory cortex. *NeuroImage* 34,
943 264–273.
- 944 Mazziotta, J., Toga, A., Evans, A., Fox, P., Lancaster, J., Zilles, K., Woods, R., Paus, T., Simpson,
945 G., Pike, B., 2001. A probabilistic atlas and reference system for the human brain: In-
946 ternational Consortium for Brain Mapping (ICBM). *Phil. Trans. B* 3560 (1412), 1293.
- 947 Moerel, M., De Martino, F., Formisano, E., 2012. Processing of natural sounds in human au-
948 ditory cortex: tonotopy, spectral tuning, and relation to voice sensitivity. *J. Neurosci.*
949 320 (41), 14205–14216.
- 950 Morosan, P., Rademacher, J., Schleicher, A., Amunts, K., Schormann, T., Zilles, K., 2001.
951 Human primary auditory cortex: cytoarchitectonic subdivisions and mapping into a
952 spatial reference system. *NeuroImage* 130 (4), 684–701.
- 953 Rohkohl, C., Engel, K., 2007. Efficient image segmentation using pairwise pixel similarities.
954 In: Hamprecht, F., Schnörr, C. (Eds.), *Proc. 29th DAGM Symposium, Volume 4713 of*
955 *LNCS*. Springer, pp. 254–263.
- Schira, M.M., Breakspear, M., Tyler, C.W., Spehar, B., 2009. The foveal confluence in human
956 visual cortex. *J. Neurosci.* 290 (28), 9050–9058. 957
- Schonwiesner, M., von Cramon, D.Y., Rubsamen, R., 2002. Is it tonotopy after all?
958 *NeuroImage* 17, 1144–1161. 959
- Seewann, A., Kooi, E., Roosendaal, S.D., Pouwels, P.J.W., Wattjes, M.P., Van Der Valk, P.,
960 Barkhof, F., Polman, C.H., Geurts, J.J.G., 2012. Postmortem verification of MS cortical
961 lesion detection with 3D DIR. *Neurology* 780 (5), 302–308. 962
- Ségonne, F., Dale, A.M., Busa, E., Glessner, M., Salat, D., Hahn, H.K., Fischl, B., 2004. A hybrid
963 approach to the skull stripping problem in MRI. *NeuroImage* 220 (3), 1060–1075. 964
- Sereno, M.I., Dale, A.M., Reppas, J.B., Kwong, K.K., Belliveau, J.W., Brady, T.J., Rosen, B.R.,
965 Tootell, R.B., 1995. Borders of multiple visual areas in humans revealed by functional
966 magnetic resonance imaging. *Science* 2680 (5212), 889. 967
- Sereno, M.I., Lutti, A., Weiskopf, N., Dick, F., 2012. Mapping the human cortical surface by
968 combining quantitative T1 with retinotopy. *Cereb. Cortex.* 969 **Q11**
- Sigalovsky, I.S., Fischl, B., Melcher, J.R., 2006. Mapping an intrinsic MR property of gray
970 matter in auditory cortex of living humans: a possible marker for primary cortex
971 and hemispheric differences. *NeuroImage* 320 (4), 1524–1537. 972
- Striem-Amit, E., Hertz, U., Amedi, A., 2011. Extensive cochleotopic mapping of human au-
973 ditory cortical fields obtained with phase-encoding fMRI. *PLoS One* 6, e17832. 974
- Tahmasebi, A.M., Abolmaesumi, P., Geng, X., Morosan, P., Amunts, K., Christensen, G.E.,
975 Johnsrude, I.S., 2009. A new approach for creating customizable cytoarchitectonic
976 probabilistic maps without a template. *MICCAI* (1), pp. 795–802. 977
- Talavage, T.M., Sereno, M.I., Melcher, J.R., Ledden, P.J., Rosen, B.R., Dale, A.M., 2004.
978 Tonotopic organization in human auditory cortex revealed by progressions of fre-
979 quency sensitivity. *J. Neurophysiol.* 91, 1282–1296. 980
- von Economo, C., Horn, L., 1930. Über Windungsrelief, Maße und Rindenarchitektonik der
981 Supratemporalfläche, ihre individuellen und ihre Seitenunterschiede. *Z. Neurol. Psy-*
982 *chiatry* 130, 678–757. 983
- von Economo, C., Koskinas, G.N., 1925. Die Cytoarchitektonik der Hirnrinde des
984 erwachsenen Menschen. Springer. 985
- Wallace, M.N., Johnston, P.W., Palmer, A.R., 2002. Histochemical identification of cortical
986 areas in the auditory region of the human brain. *Exp. Brain Res.* 143, 499–508. 987
- Woods, D.L., Stecker, G.C., Rinne, T., Herron, T.J., Cate, A.D., Yund, E.W., Liao, I., Kang, X.,
988 2009. Functional maps of human auditory cortex: effects of acoustic features and at-
989 tention. *PLoS One* 4, e5183. 990
- Zilles, K., Schleicher, A., Palomero-Gallagher, N., Amunts, K., 2002. Quantitative analysis of
991 cyto- and receptor architecture of the human brain. In: Toga, A.W., Mazziotta, J.C.
992 (Eds.), *Brain Mapping: The Methods*. Academic Press. 993